Maria Rozman[1]
Department of Mechanical Engineering,
Pennsylvania State University,
State College, PA 16801
e-mail: mmr6318@psu.edu

Eric T. DeShong
Department of Mechanical Engineering,
Pennsylvania State University,
State College, PA 16801
e-mail: etd5060@psu.edu

Karen A. Thole
Fellow ASME
Department of Mechanical Engineering,
Pennsylvania State University,
State College, PA 16801
e-mail: kthole@psu.edu

Reid A. Berdanier
Mem. ASME
Department of Mechanical Engineering,
Pennsylvania State University,
State College, PA 16801
e-mail: rberdanier@psu.edu

Christopher Robak
Pratt & Whitney,
East Hartford, CT 06118
e-mail: christopher.robak@prattwhitney.com

Characterizing Flow Instabilities During Transient Events in the Turbine Rim Seal Cavity

Gas turbine engine design requires considerations not only for long-term steady operation but also for critical transient events. Aircraft engines undergo significant stress during takeoff and landing, while power generation turbines must be flexible for hot restarts as renewable energy sources come online and offline. During these transient cycles, engines sustain wear and degradation that can lead to a reduction in the lifespan of their components and more frequent, costly maintenance. Cooling flows are often used to mitigate these effects, but can lead to complex and problematic flow interactions. This study uses high-frequency response pressure probes and heat flux gauges in the rim seal cavity of a one-stage research turbine to characterize the properties of large-scale flow structures during transient operation. A continuous-duration turbine testing facility provides the ability to assess the importance of these transients by first reaching steady-state operation before imposing transient behaviors. Although previous studies have conducted similar measurements for steady purge flows and wheel speeds, varying these parameters to simulate transient effects revealed several unique phenomena not identifiable with discrete steady measurements. The measurement approach connects the varied transient parameter to the behavior of the flow structures to enable a better understanding of the type of instability observed and the root cause of its formation. In particular, a relationship between instability cell formation and rim sealing effectiveness was identified using experimental data and was supported through computational simulations. [DOI: 10.1115/1.4055748]

Keywords: cavity and leaking flows, impact on cavity leaking flows on performance, measurement techniques

Introduction

Gas turbine engines are subject to transient events whenever operating parameters such as speed, temperature, and load are varied [1]. Such transient events are present in all gas turbine applications albeit with varying degrees of severity and frequency. In aviation, frequent takeoff and landing operations are required for commercial applications [2], while military engines must respond quickly as the pilot executes evasive maneuvers. In land-based applications, such as power generation, turbines must match the shifting energy demand through the day [3]. As the implementation of renewable energy increased over the past few decades [4], this latter form of transient operation has become increasingly substantial.

There are several thermal effects that result from transient engine operation: metal heat storage, variation of coolant flow fractions, and clearance variations due to thermal expansion [5–8]. The severity of these effects on engine components and subsystems is important to understand to ensure appropriate considerations are made during engine design and operation. The thermal effects of transients are most substantial in the hottest sections of the engine—the combustor and turbine. Here, the temperature of the main gas path (MGP) flow exceeds the metal softening temperature of the hardware [9], which requires the use of cooling and sealing flows, also known as purge flows, to ensure safe operation.

In the turbine section, purge flows are used alongside rim seal geometries to prevent harmful ingestion of the MGP flow into the underplatform region—a complication that is detrimental to hardware lifespan [1,9]. At intermediate purge flowrates during the steady state, the periodic sequence of ingress and egress of MGP flow into the rim seal intensifies [10,11]. Thermal cycling accompanies pressure cycling when ingress–egress patterns are present [10], and this pattern of thermal stress can cause damage to the hardware. In addition to its importance to hardware durability, minimizing the purge flow demand is also critical to engine efficiency. The flow is diverted from the compressor; therefore, excessively high purge flow demands may result in parasitic efficiency losses, as well as turbine efficiency losses when the leakage from the cavity mixes with the MGP flow; this effect has been approximated as a 1.4% increase in efficiency for a 50% decrease in the purge flowrate [12]. Hence, it is important to understand how the rim seal cavity sealing behaves during transients.

The majority of studies investigating rim sealing performance are conducted under thermally steady conditions [11,13,14]. Although several studies have examined the effects of transient operation [7,15,16], only one to date has used experimental data to validate their computational models [15]. The present study leverages a continuous-duration test facility to address these gaps in understanding by investigating the influence of transient operation on rim seal characteristics.

Literature Review

Only a limited number of studies have used computational modeling to investigate performance variations during transient events. Nielsen et al. [7] studied transient effects in gas turbine engines by developing a computational model that calculated clearance variation in the secondary air system. May and Chew [16] used transient 1D and 2D models to demonstrate that pressure profiles and disk cavity vortices in the disk cavity were dependent on the wheel speed rotational effects. These vortices were also shown to affect the pressure at the radial inlet and outlet of the cavity, but were attenuated by the increasing purge flowrate. The model by May

et al. used a highly simplified geometry lacking blades and vanes that have been shown to have a significant impact of vortex strength in the disk cavity [17–21].

Berdanier et al. [15] used experimental methods to examine how transient purge flow influenced a variety of engine health-related factors such as thermal growth of hardware and sealing effectiveness. While their study used pneumatic pressure taps to evaluate performance, this study expands upon those methods by applying fast response instrumentation that allowed for more in-depth, time-resolved analysis. Few studies have endeavored to understand transient phenomenon. Those who have studied transient phenomena in turbomachinery left much room to explore experimental methods using engine-relevant hardware and conditions.

Although few studies have used experimental validation to examine how the cycles of ingress and egress differ during transient operation, a robust foundation has been established by numerous steady-state studies. Many foundational studies have examined the driving forces of ingestion [12,22]. Owen [23] derived analytical solutions for the flow between rotating and stationary disks. This analysis led to the categorization of the types of ingestion: rotationally induced, externally induced, and combined ingress [24,25]. Pressure measurements have been commonly used to characterize flow behaviors in the rim seal cavity, and the ability of the purge flow to prevent ingestion is often quantified using rim sealing effectiveness, a property determined by measuring the concentration of a tracer gas. Phadke and Owen [26] used a wheel space low-pressure criterion as evidence of ingress, and other articles have connected pressure variation with ingestion and sealing effectiveness [17,27]. The extent of the impact of MGP ingestion is therefore not yet well understood during transient operation.

Large-scale structures caused by fluid instabilities in the rim seal cavity have been identified by several investigations [17,28]. The formation of these instabilities, also referred to as cells, in intermediate purge flow regimes has been linked to an inflection point in the sealing effectiveness curve [11,17,19]. It is theorized that the low pressure caused by the flow structures draws the fluid from the MGP in through the rim seal, reducing the effectiveness inside the cavity and creating this inflection point [19]. One of the first to identify these structures was a study by Cao et al. [28], which used experimental methods to verify a computational fluid dynamics (CFD) model. The numerical solution visualized discrete flow structures and a frequency analysis further characterized these structures to show that they are rotating and are functions of rotor speed.

The large-scale flow structures have been identified under three main classifications: inertial waves [29], Taylor–Couette instabilities [17], or Kelvin–Helmholtz instabilities [30]. Rabs et al. [30] demonstrated that the Kelvin–Helmholtz instability vortex structure, which is generated in the shear layer between two parallel flows of different velocities, could form in the rim seal cavity at the intersection of the ingested flow and the sealing air flow. These cells are important to understand not only because they cause time-varying thermal variations but also because they can decrease the time-steady sealing effectiveness, corresponding to an elevation of hardware temperature over the course of operation. This study focuses on the Kelvin–Helmholtz instability theory about instability cell formation.

Methods have been developed to calculate the properties of these flow structures from multichannel, fast response pressure transducers. For example, Beard et al. [31] introduced cross correlating two pressure signals from the rim seal cavity to calculate the speed of the structures as they flow circumferentially about the wheel space. The structures travel consistently at about 80% of the disk speed, and the count varies with the purge flowrate. Lei et al. [32] found that the speed of the structures decreased slightly with the increasing purge flowrate and concluded that purge flow stabilizes the flow in the cavity. Monge-Concepción et al. [11] examined the effect of flow ingestion on the stability in the rim seal cavity. Their study found that the cell properties calculated from experimental data agreed with the visualization from the quarter wheel unsteady Reynolds-averaged Navier–Stokes (URANS) models

developed by Robak et al. [33]. The present article extends this instability analysis method by applying it to transient operation.

While it has been established that transient operation is particularly damaging to engines [5–9], and many studies have evaluated flow structures at steady purge flowrates or wheel speeds, no other study has used fast response instrumentation to examine the flow structure behavior during transient regimes. Therefore, the purpose of this article is to address this gap by experimentally exploring rim seal cavity phenomena during transient regimes.

Experimental Methods

This study was conducted at the Steady Thermal Aero Research Turbine (START) Lab at the Pennsylvania State University. Figure 1 depicts the major components of the facility in blue, with the colors of the arrows corresponding to the relative gas path temperatures. The design of the START facility is outlined in detail by Barringer et al. [34], and the transient operation capabilities are discussed by Berdanier et al. [15].

The research facility contains a one-stage turbine test section comprised real engine hardware and operated in a continuous-duration mode at engine-relevant conditions. The dynamometer installed at the facility allows for steady operation up to 11,000 rpm with speed setpoint stability within ±10 rpm. Supply air for the turbine is provided by two industrial compressors, each powered by 1.1 MW (1500 HP) motors, capable of a combined airflow of up to 10.4 kg/s (25 lb_m/s) with an outlet pressure of 480 kPa (70 psia) and nominal outlet temperature of 38 K (220 °F). The majority of the flow from the compressors continues into an in-line natural gas heater positioned upstream of the turbine. The combustor burns natural gas and has a maximum capability of 672 K (750 °F), although the facility was operated at a lower temperature in this study.

Approximately 10% of the flow is diverted from the MGP before it enters the combustor. This flow is cooled to 273 K (32 °F) using a shell-and-tube heat exchanger, and it then can be distributed to several injection points throughout the stage, each of which is independently controlled and metered. For this study, only purge flow was evaluated, as depicted by the blue arrow in the cross-sectional view shown in Fig. 2. The purge flow cools the wheel space and prevents hot MGP ingress into the rim seal cavity. This purge flow is injected into the vane underplatform region through 150 equally spaced holes distributed around the hardware. The facility is also capable of using the redirected flow as vane trailing edge flow and tangential on-board injection (TOBI) flow, but neither were used in this study.
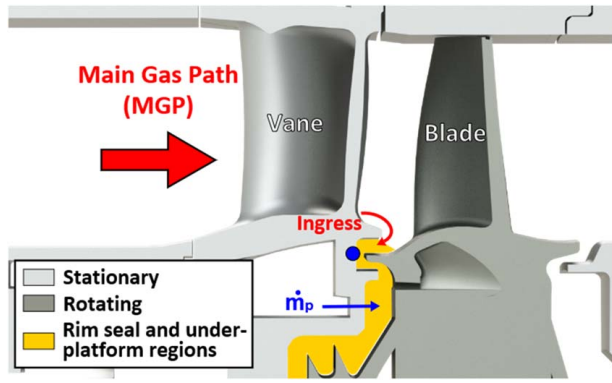

Fig. 1 Model of START facility, highlighting important components and areas of interest
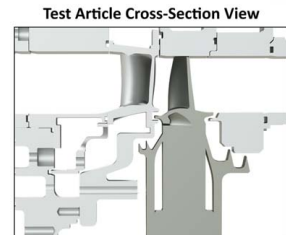
Fig. 2 Single-stage turbine and underplatform system cross section, with important parameters highlighted

Facility Instrumentation. Experimental data for this study were collected using fast response sensors installed in two additively manufactured vanes. The data collected from fast response pressure transducers, heat flux gauges (HFG), and tip clearance probes were sampled at a nondimensional sampling frequency of $f_s/f_D \approx 600$, where f_s and f_D represent the data sampling rate and the disk frequency, respectively. A low-pass filter was also applied to prevent aliasing. The calibration of these fast response pressure transducers is described in detail by Siroka et al. [10]. Six pressure transducers were installed in the rim seal cavity at radial installation locations shown by the blue circular marker in Fig. 2 and the circumferential location shown in Fig. 3. The fast response pressure sensors were distributed with equal spacing across one vane pitch, and a subset of the measurements were used for the present analysis.

This study also used the fast response temperature signal collected by one single-sided thin film HFG at the same radial location in the rim seal region, as depicted by the red triangle in Fig. 3. Other property measurements such as flowrates, speeds, temperatures, and pneumatic pressures were read using the main data acquisition system with data save rates of 1 Hz.

Rim sealing effectiveness is quantified by seeding the purge flow with a supply concentration, c_s, of 1% CO_2. Total pressure probes with Kiel heads were installed at the turbine vane inlet to measure the nominal CO_2 concentration at the turbine stage inlet, c_∞. Further concentration measurements, c, were collected at various radial locations within the rim seal for comparison. The rim sealing effectiveness is, defined by Eq. (1):

$$\varepsilon_c = \frac{c - c_\infty}{c_s - c_\infty} \tag{1}$$

is fundamentally bounded between 0, where the flow is entirely sourced from the MGP, and 1, where the flow is entirely sourced
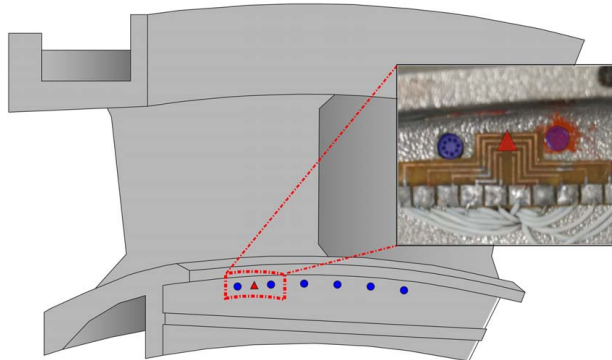
from the purge flow. Effectiveness values reported in this study were previously presented by Monge-Concepción et al. [35]. The methodology of quantifying effectiveness using gas tracing has been studied at length in the literature [18,27] and has been previously reported by the START lab [10,11,13,14,36].

Turbine Steady and Transient Operating Conditions. The data presented in this study were collected under primary operating conditions identical to Berdanier et al. [15] as described in Table 1. The purge flowrate is presented in a nondimensional form, Φ_p/Φ_{ref}, where Φ_p is the measured nondimensional purge flowrate as described in the study by Sangan et al. [37], and Φ_{ref} is the nondimensional purge flowrate at which the cavity at the coolant injection plane is fully sealed.

In addition to its primary focus as a steady research turbine, the continuous-duration nature of the START facility creates a unique ability to collect transient operation data for a number of parameters. Transient parameters of particular interest that have been evaluated in the past include purge flowrate, wheel speed, MGP temperature, and TOBI blade flow. For the purposes of this study, the response of the system to transient purge flowrate and wheel speed was characterized.

For transient purge flow operation, as depicted in Fig. 4, the entire system was initially brought to thermally steady conditions at the zero-purge flow operating condition. The purge flowrate was then increased to a high-flow condition over 90 s by opening the flow control valve from fully closed to its fully open position. The end state for the valve opening is user defined; for this study, the high-flow condition always exceeded the purge flow required to achieve a fully sealed condition in the rim seal. After the initial transient period, the system was again allowed to thermally soak at the high purge flow condition. This same procedure was followed in reverse for the decreasing purge flow transient operation, which enabled the characterization of hysteresis patterns. A more in-depth description of this procedure, transient thermal growth considerations, and their associated effect on hysteretic seal performance were reported by Berdanier et al. [15].

Similar to the transient purge flow tests, transient wheel speed operation started by achieving steady-state conditions at a

Table 1 Operating conditions

Parameters	Symbol	Value
Blade inlet axial Reynolds number	Re_x	1.4×10^5
Rotational Reynolds number	Re_Ω	3.5–6.0×10^6
Density ratio	ρ_p/ρ_{MGP}	1.0–2.5
Nondimensional purge flow	Φ_p/Φ_{ref}	0–1.5

Fig. 3 Diagram of a vane doublet showing the circumferential location of fast response probe installations
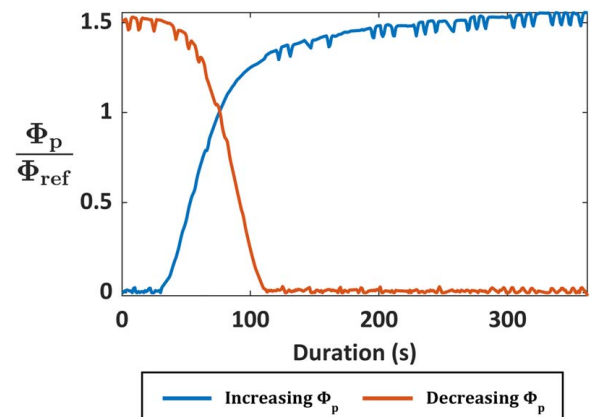

Fig. 4 Transient nondimensional purge flow as function of time

reduced wheel speed of 7000 rpm. The rotational speed was then manually increased at a fixed ramp rate up to a high-speed condition just below the 11,000 rpm facility maximum (to maintain sufficient safety buffers). After the initial ramp up of wheel speed, the system was allowed to reach a steady-state condition at the high-speed condition before passing through a fixed ramp rate decrease to the original reduced-speed condition. For consistency, the ramp rate was maintained at approximately 700 rpm per minute for both increasing and decreasing trials.

Measurement Uncertainty. All measured parameters inherently include bias and precision uncertainty. Table 2 shows the measurement uncertainty for turbine operating parameters and instrumentation. The uncertainty calculation method applied to all data and calculations contained within this study is described in the study by Figliola and Beasley [38]. The data are presented using normalized pressure P', temperature T', nondimensional frequency f/f_D, normalized cell speed (Ω_S/Ω_D), and cell count (N_S). This article follows the normalization method established by DeShong et al. [39] for pressure and temperature data, which are presented as self-normalized differences using the minimum and maximum values from the transient purge flowrate dataset. This normalization procedure is defined in Eq. (2).

$$X' = \frac{X - X_{min}}{X_{max} - X_{min}} \tag{2}$$

Nondimensional Transient Purge Flow

Previous studies investigating rim sealing have primarily used the nondimensional purge flowrate Φ_p when detailing the independent variable, which was derived as a function of nondimensional flow rate, seal clearance ratio, and rotational Reynolds number [24,25,37,40]. As shown in Eq. (3), Φ_p is a function of purge flowrate, seal clearance, density, rotational velocity, and radial location:

$$\Phi_p = \frac{\dot{m}_p}{2\pi s_c \rho \Omega_D b^2} \tag{3}$$

where $\dot{m}_p$ is the purge flow rate, s_c is the sealing clearance, ρ is the density, Ω_D is the disk frequency, and b is the hub radius.

The parameter Φ_p is derived from an orifice model, which includes an analytical solution and has demonstrated agreement with experimental data. Nondimensional purge flowrate Φ_p is proportional to purge flowrate $\dot{m}_p$ for specified seal geometries and operating conditions; therefore, they can often be used interchangeably, and relationships such as $\dot{m}_p/\dot{m}_{ref}$ and Φ_p/Φ_{ref} are equivalent; this equivalence is only valid for thermally soaked steady-state operation. For transient operation, several studies have shown that clearance varies [5–7,15]. For this study, the seal clearance was not measured directly, but was estimated using Eq. (4) [15]:

$$s_c = r_{1a} + r_{s,t0}\alpha(T_2 - T_{t0}) - (\tau - \tau_{t0}) \tag{4}$$

where r_{1a} is the design rim seal clearance, $r_{s,t0}$ is the initial value, α is the coefficient of thermal expansion, T_2 is the measured metal

Table 2   Measurement uncertainty

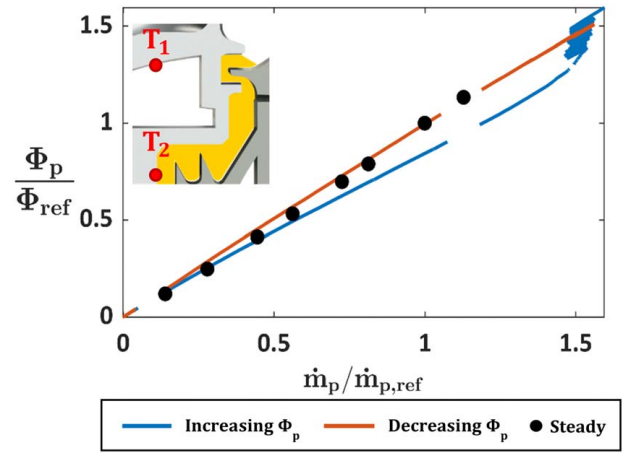| Parameters	Symbol	Uncertainty
Shaft rotational speed	Ω/Ω_{ref}	±0.001
Purge flowrate	Φ_p/Φ_{ref}	±0.018
Inlet pressure	P'_{in}	±0.002
Inlet temperature	T'_{in}	±0.001
Time-resolved pressures	P'/P_{ref}	±0.030 to ±0.127
Time-resolved temperatures	T'/T_{ref}	±0.005 to ±0.021
Sealing effectiveness	ε_c	±0.015 to ±0.025
Rotor tip clearance	τ/r_s	±0.0001

Fig. 5   Nondimensional purge flowrate, Φ_p/Φ_{ref}, as a function of normalized purge flowrate $\dot{m}_p/\dot{m}_{p,ref}$ calculated using T_2

temperature, T_{t0} is the initial temperature at the beginning of a transient event, τ is the measured blade clearance, and τ_{t0} is the initial clearance. The nomenclature T_2 is used for consistency with the study by Berdanier et al. [15]. The first term in this equation accounts for the initial seal clearance, the second accounts for dimensional changes of the stator due to thermal expansion, and the third approximates the thermal growth of the rotor, as defined in the study by Berdanier et al. [15].

During transient operation, the changing seal clearance behavior dictates Φ_p, which was calculated for this study using nonconstant values of ρ and seal clearance s_c as shown in Eq. (4). As previously identified, the calculation of s_c is dependent on the selection of temperature for use in Eq. (4) [15]. For this reason, the corresponding effect of temperature selection and its influence on relationships between $\dot{m}_p/\dot{m}_{ref}$ and Φ_p/Φ_{ref} were evaluated.

Two options were considered for the selection of the temperature variable, corresponding to two locations in the underplatform region. The impacts of, and supporting justification for, calculating the sealing clearance using one of these two temperatures is described in the study by Berdanier et al. [15].

Figure 5 depicts the radial locations of the two temperature sensor options as well as the resulting Φ_p/Φ_{ref} for the preferred temperature measurement. A pattern of hysteresis is shown between the two transient trials with the steady data closely following the decreasing purge flowrate trial data. Based on this behavior, the decreasing purge flow trial is a better approximation of thermally soaked conditions, due to the system reaching steady state at maximum purge flow conditions. The calculation method shown in Fig. 5 using the inboard temperature location T_2 is used for the remainder of this article, as it reflects a matched relationship between the decreasing transient trial and the steady data.

Temperature Hysteresis Effects

An important parameter that dictates thermal lag and flow behaviors in the rim seal cavity is the temperature difference between the MGP and the purge flow, as defined in Eq. (5).

$$\Delta T = T_{MGP} - T_p \tag{5}$$

Figure 6 shows the behavior of the driving temperature difference $\Delta T'$ normalized using the scheme defined in Eq. (2) during the increasing, decreasing, and steady purge flowrate trials. These hysteresis effects are representative of the thermal lag that would also be present during transient events in true-scale engine operation.

The increasing trial has a very low $\Delta T'$ because it starts from a zero-purge operating condition. The purge supply hardware was allowed to come to a high steady-state temperature because there

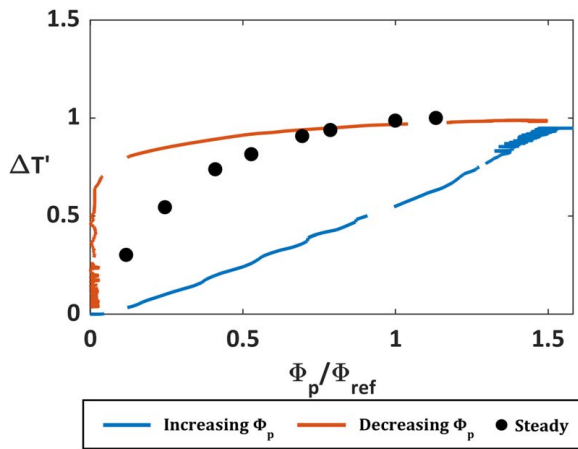**Fig. 6 The driving temperature difference as a function of non-dimensional purge flowrate showing hysteresis**

Fig. 7 Fast response pressure and temperature signals for one revolution at $\Phi_p/\Phi_{ref} = 0.7$

was no purge flow to cool it. As the purge flow is increased, the hot hardware transfers heat into the purge flow before it reaches the disk cavity, which greatly decreases the temperature differences between the purge and MGP flows.

After the end of the increasing purge flow, the system is maintained at the maximum purge flow condition and allowed to reach steady-state again. During that period, the hardware cools to its minimum temperature. When the purge flow is subsequently decreased, the cool hardware acts as a heat sink and the $\Delta T'$ remains high even at low purge flowrates. This thermal lag can be observed when comparing the steady-state points in Fig. 6 to the transient operation lines. The $\Delta T'$ of the steady and decreasing trial data far exceed that of the increasing trial data because the system is nearly thermally soaked during the decreasing trial, while the steady purge condition is completely thermally soaked. At low purge flowrates, however, the steady $\Delta T'$ is exceeded by the decreasing purge transient, as the hardware does not have enough time to heat up to match its temperature under thermally steady conditions. The same analysis shown in Fig. 6 was also performed for transient wheel speed trials, but those trials exhibited negligible thermal lag, and therefore, $\Delta T'$ is constant with respect to rpm.

The behavior identified in Fig. 6 further influenced the selection of parameters used to calculate Φ_p—the steady data in Fig. 5 aligned with the decreasing trial when T_2 was used to calculate s_c and did not when it was calculated using T_1. To most appropriately represent the system, an accurate hysteretic relation must be preserved.

Unsteady Pressures and Analysis

Fast response pressure and temperature sensors were used to capture the highly unsteady behavior of the Kelvin–Helmholtz-like instabilities present in the rim seal cavity observed in literature [10,17,30,32]. Previous studies have used the coefficient of pressure, C_p, whereby the pressure signal is nondimensionalized using the dynamic pressure [10,11,35]. Dynamic pressure is a function of tangential velocity and is varied during the transient wheel speed tests. Using a nonconstant parameter to nondimensionalize the data alters the trend in the time-resolved signals. To compare the pressure and temperature trends independently for transient purge flowrate and wheel speed, a constant variable was used for the nondimensionalization according to Eq. (2).

Figure 7 shows the normalized, time-resolved pressure and temperature signals for a single revolution at $\Phi_p/\Phi_{ref} \approx 0.7$. The time series data shown in Fig. 7 have been filtered using a low-pass filter to exclude the blade passing frequency, as described in the study by Monge-Concepción et al. [11]. Through this approach, the periodic behavior in Fig. 7 indicates cell passing events.
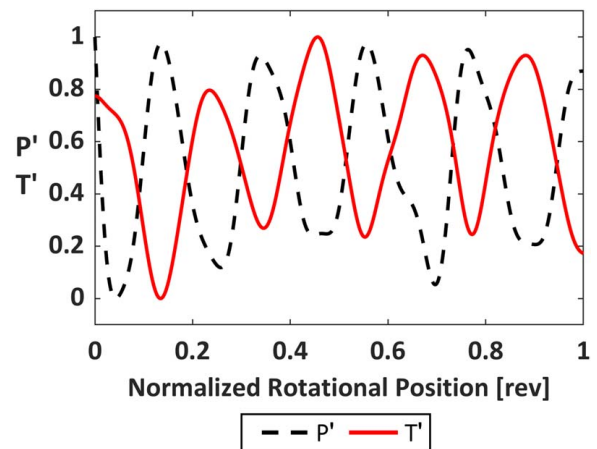
The superimposed fast response temperature data plotted in Fig. 7 are also phase shifted by approximately half a period relative to the pressure data. The cycles of low- and high-pressure during ingress and egress respectively are associated with cycles of high and low temperature—a phenomenon that was first identified by Siroka et al. [10].

Using the time-resolved data, the unfiltered pressure and temperature signals were processed using the procedure outlined in Fig. 8. This procedure generates a spectrogram-style plot, which is commonly used as an exploratory tool in acoustical analyses for transient processes. From the spectrogram-style plots, the dominant
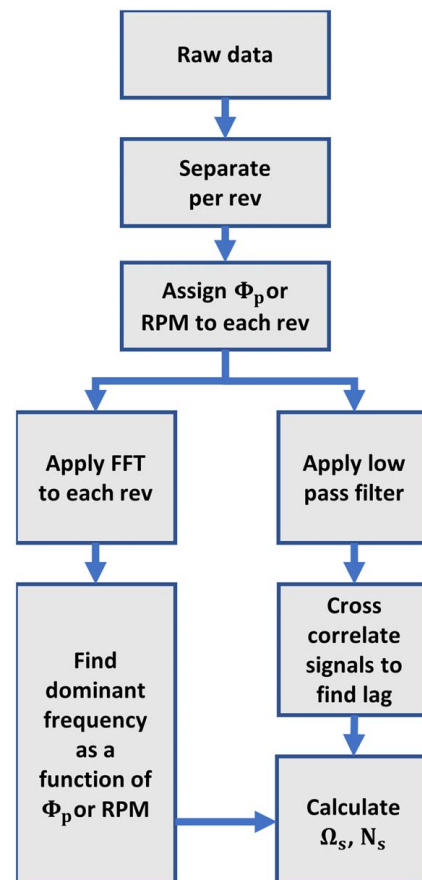

Fig. 8 Data processing flowchart

frequency and maximum amplitude are extracted as functions of the transient variable.

By using the method established by Beard et al. [31], the dominant frequency as well as the phase lag between two signals can be used to calculate cell properties, such as speed and count. The phase lag is calculated using the cross correlation of two sensors of a known spacing and is equivalent to the cell travel time between the two sensors.

Transient Frequency Domain Analysis

A comparison of steady to transient data from a transient purge flow test where the wheel speed is kept constant just below the 11,000 rpm facility maximum is shown in Fig. 9. The steady data studies that examined effects of purge flowrate similarly applied a fast Fourier transform (FFT) but did so to a dataset that spanned numerous revolutions. This method for the steady data [11], shown in the solid lines in Fig. 9(a), results in much narrower frequency bins and a more discrete dominant pressure frequency peak than in the case of the transient data.

When the FFT is applied only to a single revolution of data, the resulting frequency bin size is wider due to the shorter time series length. This effect is visible in the dashed lines in Fig. 9(a), where an FFT was applied individually to 500 revolutions of data with the resulting spectral values being ensemble averaged. Despite the wider lobes, the peak is centered at the same frequency, as is expected. It should also be noted that the two datasets featured in Fig. 9(a) were normalized using local maxima and minima, so the amplitudes are not intended to be a point of comparison.

For the purposes of a transient analysis, there may be changes occurring between revolutions, so applying an FFT to the entire dataset does not allow for detection of such events. In Fig. 9(b), the revolution-by-revolution FFT method is applied to a transient dataset at a selection of discrete purge flowrates matching the steady dataset. Qualitatively, the transient frequency spectra in Fig. 9(b) are nearly identical to the dashed lines in Fig. 9(a), which shows the similarity between the transient and steady data at equivalent nondimensional purge flowrates. Therefore, when analyzing the transient datasets, each revolution can be assigned a discrete value, and FFTs may be displayed together as a function of the transient parameter in the style of a spectrogram plot.

Figure 10 depicts the results of the spectrogram analysis method for the transient purge flowrate trials. For brevity, only the increasing transient purge flowrate data sourced from the fast response pressure sensors are plotted in Fig. 10. The dark region spanning from $0.9 < \Phi_p/\Phi_{ref} < 1$ represents a time period where no data were collected due to a limitation in the data acquisition method. Notably, there is an abrupt shift in the dominant frequency at $\Phi_p/\Phi_{ref} \approx 0.7$. Although initially appearing discontinuous, this transition takes place over approximately 20–30 revolutions. The abrupt shift in dominant frequency was present in all data sets with repeatable behaviors present in both increasing and decreasing directions; the shift was also identified similarly in both time-resolved pressure and temperature measurements.

The dominant frequency near $f/f_D \approx 5$ shown in Fig. 10 represents the number of times per revolution an instability cell passes a sensor in the rim seal cavity. This cell passing rate is visible in the waveform data shown in Fig. 7, where there are approximately five periods in both the fast response pressure and temperature signals. The shift in this frequency illustrated by the spectrogram indicates that the number of cells passing the sensor per revolution has shifted. The shift can be due to changes in either the speed at which the cells were rotating or the number of cells distributed about the casing. The secondary frequency peak near $f/f_D \approx 10$ represents a harmonic of the fundamental frequency identified at $f/f_D \approx 5$.

Results in Fig. 11 are extracted from the spectrograms for all transient test conditions. Figure 11 also depicts the relevant distinguishing features between datasets for steady and transient conditions including both increasing and decreasing purge flows. Furthermore, data collected using fast response pressure transducers are shown in Figs. 11(a) and 11(b) and using fast response temperature sensors are shown in Figs. 11(c) and 11(d).

The maximum amplitude in Fig. 11(a) from both of the transient purge trials, the maximum amplitude in Fig. 11(c) for the decreasing purge trial, and the dominant frequencies in Figs. 11(b) and 11(d) from both the transient trials fall within the range bars from the steady-state data collected by Monge-Concepción et al. [11] and Siroka et al. [10] for the fast response pressure and temperature data, respectively. Hysteresis is observed between the increasing and decreasing transient purge flowrate trials as shown in Fig. 11, where the maximum P' amplitude for increasing purge data is reached at a lower relative purge flowrate than for the decreasing purge case. In Fig. 11(a), all three datasets align at low purge
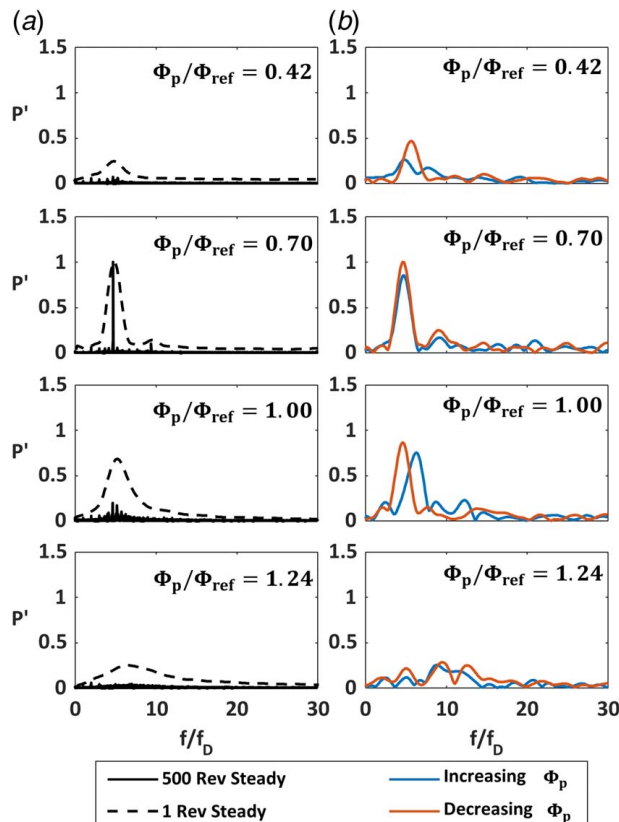

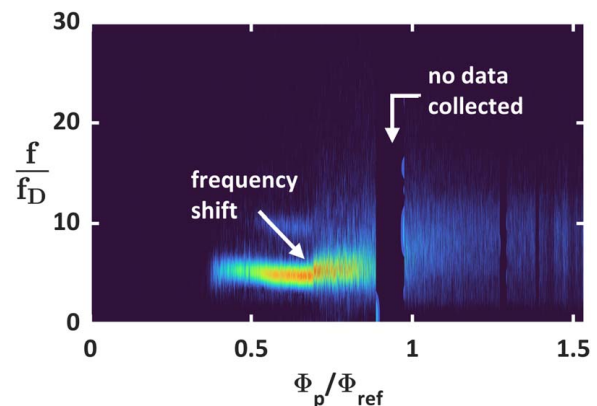Fig. 9 FFT comparison method: (a) steady data and (b) transient data

Fig. 10 Spectrogram-style plot for increasing transient purge flowrate fast response pressure sensor data
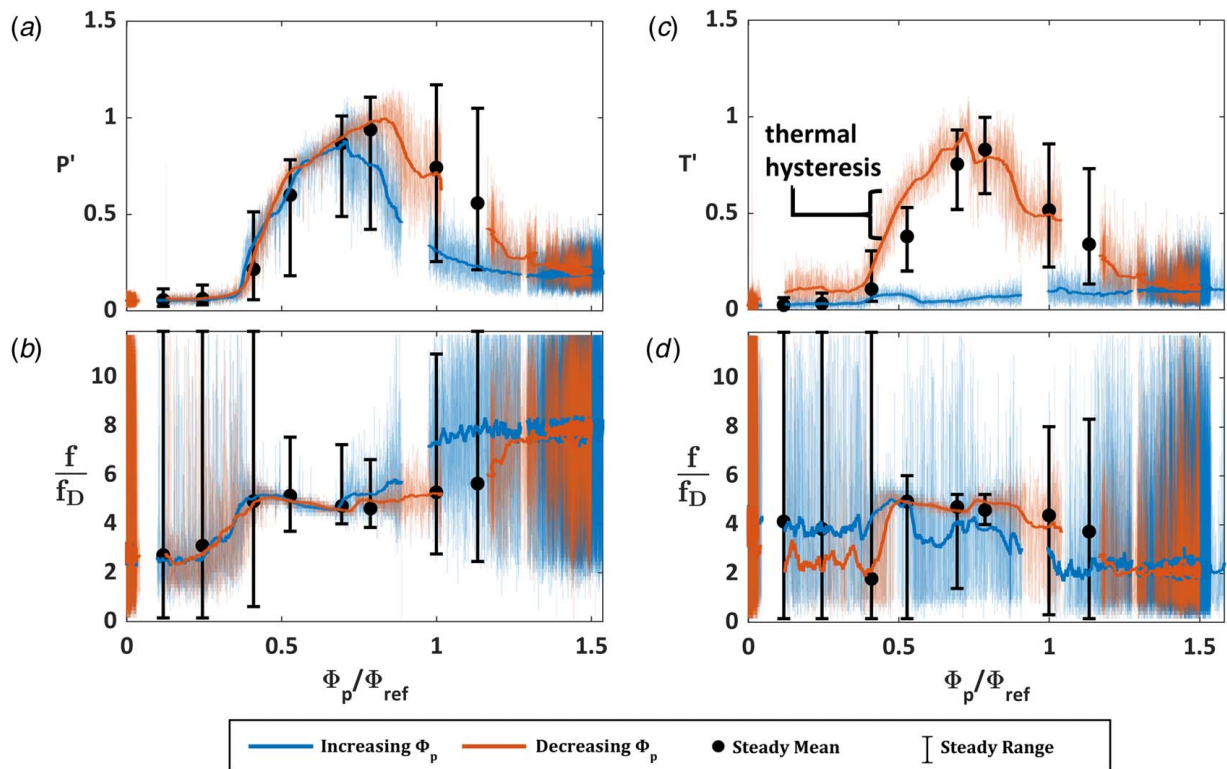
Fig. 11 (*a, c*) Maximum amplitude and (*b, d*) dominant frequency during a transient purge flow test from fast response pressure sensor (*a, b*) and temperature sensor (*c, d*) data, respectively

flowrates, but the transient data for the increasing purge case diverge at high purge flowrates from both the steady and decreasing transient data. Berdanier et al. [15] concluded from low-frequency pressure measurements that effectiveness is higher in an increasing, transient purge flow regime compared to a steady regime. This effect is due to thermal expansion in the blades during a transient process that starts with a minimal cooling flow creating a smaller sealing clearance, and thus requiring less flow to seal, reaching a fully purged condition at a lower purge flowrate. In Fig. 11(*a*), there is some hysteresis between the increasing and decreasing purge flow trials, where the amplitude of the increasing trial drops off at a lower purge flowrate than the decreasing trial. Specifically, the increasing trial reaches the same amplitude at $\Phi_p/\Phi_{ref} \approx$ 0.8 that the decreasing and steady trials do at $\Phi_p/\Phi_{ref} = 1.0$, which is consistent with the findings from Berdanier et al. [15]. Also featured in Fig. 11(*b*), both the dominant frequency shift and the high-variability frequency region associated with the amplitude decline ($\Phi_p/\Phi_{ref} > 1$) occur at slightly lower purge flowrate in the increasing trial than in the decreasing trial.

The dark region in the dominant frequency at $\Phi_p/\Phi_{ref} < 0.4$ shown in Fig. 10 does not correspond to missing data, but rather to a signal with a very low amplitude and therefore a low signal-to-noise ratio (SNR). The correspondence can be noted in the same Φ_p/Φ_{ref} range in Figs. 11(*a*) and 11(*b*).

For the temperature measurements in Fig. 11(*c*), there is significant hysteresis between the transient increasing purge flow case compared to the steady and decreasing purge flow cases. While the decreasing and steady purge cases show the same behavior as shown in Fig. 11(*a*), the increasing case shows a much lower amplitude of T'. Meanwhile, the decreasing purge data show good agreement with the steady data at high purge flowrates, but diverges at purge flowrates $\Phi_p/\Phi_{ref} < 0.75$. Both of these divergences are due to thermal lag in the system.

The hysteresis between the two transient cases in Fig. 11(*c*) is due to the driving temperature difference ΔT between the MGP and purge flow temperatures, as defined in Eq. (5) and depicted in

Fig. 6. The discrepancy between increasing and decreasing trials in Fig. 11(*c*) could be interpreted as a different ingestion behavior. However, it is important to point out that the pressure data (Fig. 11(*a*)) were collected simultaneously with the temperature data (Fig. 11(*c*)). Therefore, it is known that the flow behavior creating the trend in the increasing purge case in Fig. 11(*a*) is also occurring in Fig. 11(*c*), but is not being detected. While the pressure in the cavity cycles between high pressures during egress and low pressures during ingress, there is an analogous occurrence between thermal cycling of low temperature during egress and high temperature during ingress, as depicted in Fig. 6. However, if the MGP and purge flows are approximately the same temperature, the fast response temperature sensor is unable to distinguish ingress from egress because the ingress and egress flows are the same temperature, so the SNR is insufficient.

Conversely, as shown in Fig. 6, the driving temperature difference from the decreasing purge flow case exceeds that of the steady case at low purge flowrates. The consequence of this relation is identified explicitly in Fig. 11(*c*), where the maximum amplitude of the decreasing purge flowrate trial agrees with the steady data at high purge flowrates, but exceeds the steady data at low purge flowrates.

Due to the low amplitude from the increasing purge and the resulting low SNR, the frequency data in Fig. 11(*d*) for the increasing purge are dominated by noise. However, the decreasing purge data and the aforementioned dominant frequency shift agree with the fast response pressure signal results in Fig. 11(*b*). This consistency demonstrates that the unsteady phenomenon can be detected by both pressure and temperature sensors in the time and frequency domains.

The data from the transient wheel speed case are shown in Fig. 12. In these tests, constant dimensional purge flowrate was set to match the nondimensional purge flowrate of $\Phi_p/\Phi_{ref} = 0.7$ from the transient purge flow tests. Unlike the transient purge cases, the transient wheel speed case does not exhibit any abrupt shifts in the dominant frequency. In addition, both the datasets
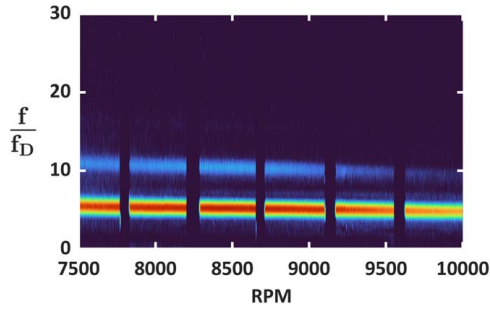
Fig. 12 Spectrogram-style plot for increasing transient wheel speed fast response pressure sensor data
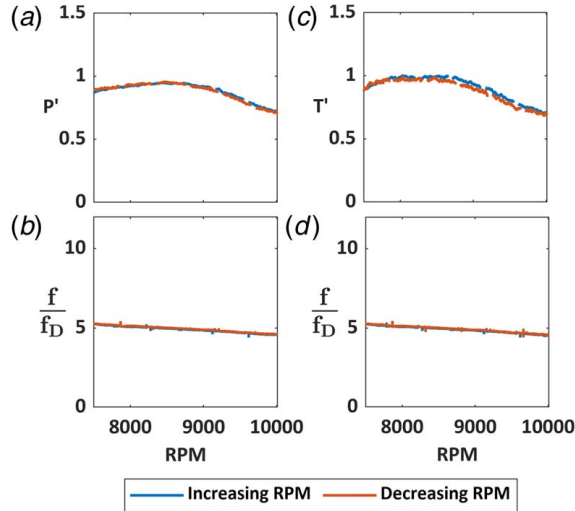

Fig. 13 (a,c) Maximum amplitude and (b, d) dominant frequency during a transient wheel speed test from fast response pressure sensor (a, b) and temperature sensor (c, d) data, respectively

result in qualitatively identical plots because they were collected concurrently from the two sensor types and captured the same phenomenon. For the sake of brevity, only the pressure data for the increasing transient wheel speed trial are shown in Fig. 12.

When the maximum amplitude and dominant frequency are extracted from the spectrograms and shown in Fig. 13, a repeatable, low variation trend in both the maximum amplitude and dominant frequency emerges. Similar to prior data presentations, the values shown in Fig. 13(a) were normalized relative to the minimum and maximum transient purge flow trial values, so as to emphasize the relatively low-amplitude variability compared to the purge flow transients in Fig. 11(a). The lack of similar hysteresis effects shown in Fig. 11(c) for the transient wheel speed cases in Fig. 13(c) is due to negligible variation in the driving temperature difference as a function of wheel speed. As previously stated, there are no abrupt shifts in the dominant frequency in either Fig. 13(b) or Fig. 13(d), but rather a linear, downward trend.

Transient Instability Cell Properties

Previous studies that have used frequency domain analysis to calculate instability cell properties focused on steady-state operation. The current study provides the ability to use the same method for the transient purge data. The time required for a cell to pass between sensors is determined by cross correlating the signals of two sensors some known angle apart. It should be noted that this analysis was only conducted using the fast response pressure sensors. Of the fast response temperature sensors installed, only

one was able to provide usable data. This calculation requires two signals, and therefore, this calculation could not be conducted on the temperature data. Similar to past studies, the time lag (Δt) and angle of separation (α_k) are combined in Eq. (6) to calculate cell speed [11,31].

$$\Omega_s = \frac{\alpha_k}{\Delta t} \quad (6)$$

The cell speed Ω_s normalized by disk speed Ω_D is shown in Fig. 14 as a function of transient purge flowrate. The cell properties are functions exclusively of data depicted in Figs. 7 and 11(b). It has already been established that the steady data aligns with the transient data; therefore, it is also appropriate to conclude that the calculated cell properties agree between the steady and transient datasets. As previous studies have reported, Ω_s decreases with the increasing purge flowrate [11,32]. This functional relationship indicates a high purge flow stabilizes the rim seal cavity when it is nearly fully purged. As the flow stabilizes at high purge flowrates, the deceleration of the cell speed approaches zero, thereby resulting in a constant value with respect to Φ_p/Φ_{ref}. This steadily declining cell speed begins in Fig. 14 after a threshold of $\Phi_p/\Phi_{ref} \approx 0.4$. However, the values preceding this threshold are not true estimates of cell speed due to the low-amplitude pressure signals, resulting in an unreliable cross correlation.

As an additional metric assessing cell behavior, Eq. (7) uses the calculated cell speed with the dominant frequency (f_{peak}) to calculate the number of cells, N_s.

$$N_s = \frac{2\pi f_{peak}}{\Omega_s} \quad (7)$$

The number of cells is overlaid with the time-steady sealing effectiveness as a function of Φ_p/Φ_{ref} in Fig. 15.

An advantage of the presented transient analysis method is the ability for properties to be observed over a continuous variable. In Fig. 15, the cell count, N_s, is split into three separate regimes: region (I) low and noisy at low purge flowrates, region (II) constant and very discrete at intermediate purge flowrates, and region (III) high and noisy at high purge flowrates. Knowing the dominant frequency behavior in Fig. 11, cell speed values are most accurate in region (II). The others were derived from a very low-amplitude dominant frequency and are overcome by noise, as well as indicating low cell strength.

The shift in dominant frequency noted in the dominant frequency plots and spectrograms are shown in Fig. 15 as a step increase in N_s for both the increasing and decreasing transient cases. The event occurs within the same narrow Φ_p/Φ_{ref} range of about 0.65 to 0.8 repeatedly in both the increasing and decreasing purge flowrate data trials, always corresponding to an increase of one cell. These
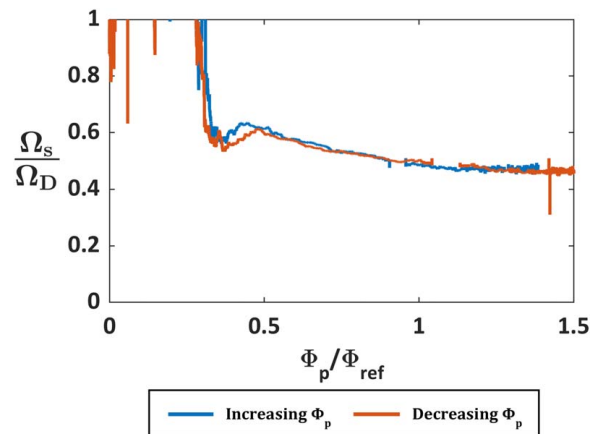

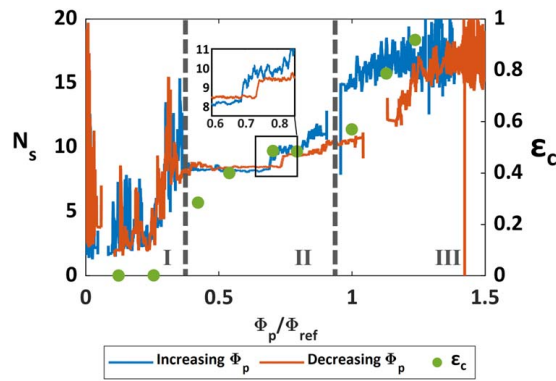**Fig. 14 Cell speed as a function of nondimensional purge flowrate**

Fig. 15 Cell count, its correlation with effectiveness, and designation of regions I, II, and III
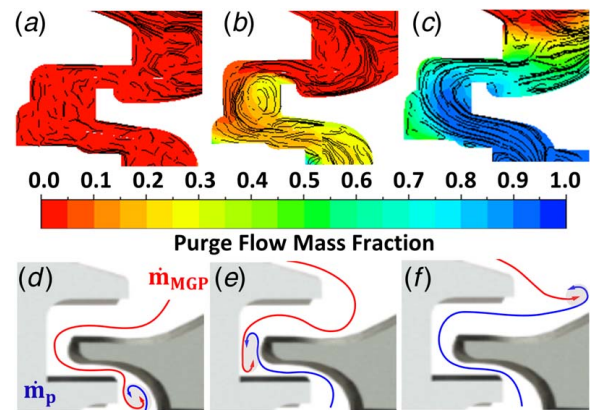

Fig. 16 Purge flow mass fraction with overlaid cavity streamlines in (a) region I, (b) region II, and (c) region III with accompanying illustrations using general geometry (d–f)

data imply that there is a purge flow threshold after which the instabilities in the cavity experience a spontaneous "cell generation event," whereupon N_s is increased by one.

The data in Fig. 15 also highlight a purge flow region in which many have reported an inflection point in the sealing effectiveness trend [11,14]. Several studies have connected the formation of instabilities in the rim seal cavity with this inflection point [17,19]. For example, Graikos et al. [19] theorized that the low-pressure regions created by the instability cells causes a pressure gradient that draws MGP flow into the rim seal cavity. The identified increase in the cell count for the transient cases—at the same purge flow range where an inflection point occurs in the sealing effectiveness—further corroborates a change in the flow physics. If the inflection point is indeed caused by the low-pressure cells drawing hot MGP air into the cavity, this effect would likely be exacerbated by an additional instability cell and attenuated as additional purge flowrate stabilizes the region. The hypothesis is that the instability transitions from increasing in strength to decreasing in strength, which implies conditions transition from favorable, where formation of the instability is supported, to nonfavorable, where the flow in the rim seal cavity is stabilizing. This critical region containing both the highest cell coherence and inflection point is accompanied by the cell generation event, which further supports the idea that the instability is undergoing a transition that is driven by the changing flow conditions in the wheelspace.

The separation of Fig. 15 into three separate operating regimes is further supported by CFD simulations [11,33], accompanied by corresponding illustrations of the flow structure behavior in Fig. 16. The CFD results shown in Figs. 16(a)–16(c) were generated using the same methodology as a URANS CFD study by Robak et al. [33], which used a quarter wheel geometry and periodic boundary conditions. The solution was validated using experimental data from the START facility. It should be noted that while Figs. 16(a)–16(c) show a simulation conducted using test facility representative geometry, Figs. 16(d)–16(f) show an illustration using general geometry. The CFD solution is depicted in Figs. 16(a)–16(c) using a purge flow mass fraction contour to illustrate MGP ingestion and is overlaid with cavity streamline to further emphasize the flow structures.

Region I is defined at low purge flowrates in Figs. 16(a)–16(d), and the entire rim seal cavity is flooded with the hot MGP flow. For these conditions, the purge flowrate is too low to seal the rim seal region, and the purge flow instead exits the underplatform region through leakage paths [33]. Figures 16(a) and 16(d) also show that interaction between the MGP and purge flows in region I occurs radially inboard from the rim seal location. Moreover, there are no instability cells formed in this regime, supported by the dark region with a low-amplitude dominant frequency around $f/f_D \approx 5$ at $\Phi_p/\Phi_{ref} < 0.4$ shown in Fig. 10.

At the opposite end of the transient test, Figs. 16(c) and 16(f) depict region III, defined by high purge flowrates where the

cavity is mostly purged of MGP flow and shear interactions are occurring on the main gas path-side outboard of the rim seal. The lack of cell formation within the rim seal is also supported by the low-amplitude dominant frequency region at $\Phi_p/\Phi_{ref} > 1.1$ in Fig. 10. While this operation range would ensure that the disk cavity is kept cool and free of the MGP flow, it is also inefficient. The high purge flowrate leads to parasitic losses due to excessive flow bled from the MGP, as well as mixing and cooling losses as leakage from the cavity interacts with MGP.

In the middle, region II is defined by the formation of a discrete, vortical instability in the rim seal cavity at intermediate purge flowrates. Figures 16(b) and 16(e) specifically visualize how the MGP flow is drawn into the wheel space. This behavior occurs in the region characterized by the stable dominant frequency for
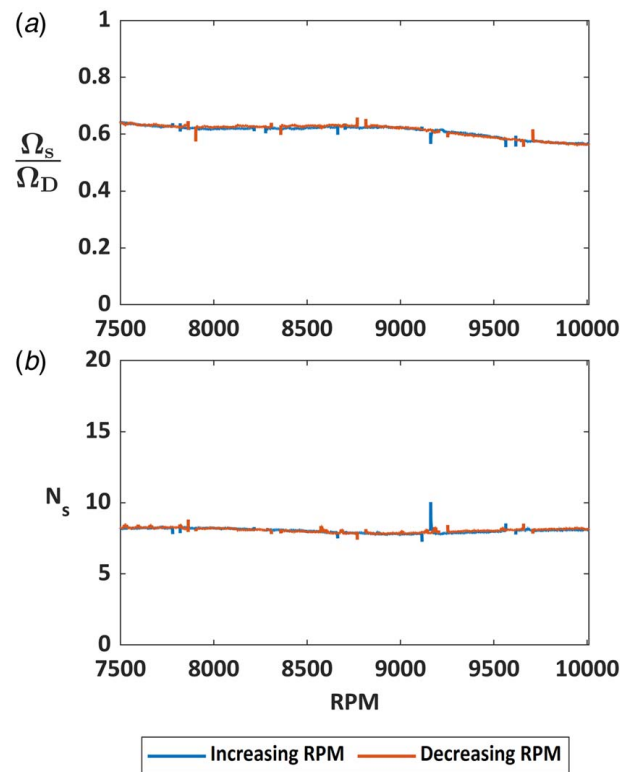

Fig. 17 Transient wheel speed trial (a) cell speed and (b) cell count

$0.4 < \Phi_p/\Phi_{ref} < 1.1$ (Fig. 10), at the center of which the cell generation event occurs. Region II also coincides with the high amplitude region of Fig. 11(a), meaning the high SNR of the fast response signals and the resulting clear dominant frequency are indicative of high instability cell coherence.

The cell properties from the transient wheel speed trials are depicted in Fig. 17. The cell speed shows a slight decreasing trend with the increasing wheel speed, but the cell count, N_s, remains constant, apparently contradicting studies that have shown that ingestion can be induced by rotational effects [24]. It was noted in the discussion about Figs. 13(b) and 13(d) that the dominant frequency as a function of wheel speed had a slight decreasing trend. In Eq. (7), the division of decreasing dominant frequency by decreasing cell speed causes the resulting constant cell count. While the constant cell count trend may be interpreted to suggest that flow instabilities are not functions of wheel speed, it is possible that the shear interaction between purge and MGP flow dominates over the rotational effects. Any transient shear effects due to change in relative velocity in the mid-stage region due to change in the wheel speed must also therefore be negligible.

The purge flowrate of the transient wheel speed trials lies within region II, where the instability cells are at their maximum coherence. The magnitudes of both of the cell properties shown in Fig. 17 are consistent with region II shown in Figs. 14 and 15, respectively, from the transient purge flowrate trials. This supports the claim that purge flowrate in region II has a greater impact than wheel speed on cell properties. Further studies are required to determine if rotational effects are still negligible with respect to shear effects in other purge flow regimes.

Conclusions

This study leverages the unique capabilities of the continuous-duration test article at the START lab to examine the effects of transient purge flowrate and wheel speed on the flow structures in the rim seal cavity of a single-stage turbine. The measurements were collected using fast response pressure and temperature sensors to examine time-resolved events. Flow behaviors identified in the measurements were further supported by visualization from CFD simulations.

A frequency analysis was conducted on a revolution-by-revolution basis, which reveals trends as functions of transient independent variables. Through the use of a spectrogram-style plot, unique transient phenomena were identified at the frequency of the underplatform instability behavior. Namely, a shift in the dominant frequency was observed repeatedly during the transient purge flowrate trials. Conversely, this analysis method indicated that the frequency of these flow instabilities is constant with respect to the wheel speed, implying shear effects from the interaction between purge and main gas path flow dominate over rotational effects from the wheel speed at intermediate purge flowrates.

Significant hysteresis between the increasing and decreasing trials was present in the fast response temperature measurements for the transient purge flowrate dataset but not the transient wheel speed dataset. This discrepancy shows that the hysteresis was induced by thermal lag between the system hardware and the cooling purge flow. Similar behaviors were not present during the transient wheel speed trials, where the system was thermally soaked throughout the entire test campaign.

Finally, the flow instabilities in the rim seal cavity were characterized by determining the cell speed and count from the dominant frequency and cross correlations of multiple pressure signals. Through this analysis, the identified shift in the dominant frequency of the transient purge flowrate was connected to an increase of one instability cell, typically occurring over the range of 20–30 revolutions. The identified change in N_s was also associated with a known inflection point in the rim sealing effectiveness as a function of purge flowrate, indicating that the sudden generation of a low-pressure flow instability draws MGP air into the wheel space.

The results of this study serve to expand upon all previous research endeavors into the topic of underplatform flow instabilities and to explore the behaviors of instabilities during transient processes. These observations will benefit future engine designers in improving engine efficiency and hot section component lifespan by understanding the types of flow phenomena that may be caused by transient operation.

Conflict of Interest

There are no conflicts of interest.

Data Availability Statement

The datasets generated and supporting the findings of this article are obtainable from the corresponding author upon reasonable request.

Nomenclature

b = hub radius
f = frequency
t = time
N = count
P = pressure
T = heat flux gauge temperature
$\dot{m}$ = mass flowrate
r_{1a} = design rim seal clearance
r_s = dimension rim seal clearance
s_c = sealing clearance
C_p = coefficient of pressure, $(P - \bar{P})/0.5\rho\Omega^2 b^2$
Re_x = axial Reynolds number $V_x C_x/\nu$
Re_Ω = rotational Reynolds number $\Omega_D b^2/\nu$
PR = pressure ratio, P_{in}/P_{out}
ΔT = driving temperature difference

Greek Symbols

α = coefficient of thermal expansion
α_k = angle between pressure transducers
ε_c = rim sealing effectiveness
ρ = density
τ = tip clearance
ν = kinematic viscosity

Φ = nondimensional purge flowrate
Ω = angular velocity

Subscripts and Accents

0 = initial
1,2 = measurement locations
D = disk
in = inlet conditions
max = maximum quantity
min = minimum quantity
out = outlet conditions
p = purge
peak = maximum value per dataset
ref = reference condition
s = instability cell
x = axial direction
$\bar{X}$ = mean quantity
X' = quantity normalized over single test conditions

References

[1] Meher-Homji, C., and Bhargarva, R., 1994, "Condition Monitoring and Diagnostic Aspects of Gas Turbine Transient Response," Int. J. Turbo Jet Eng., **11**(1), pp. 99–111.

[2] Tona, C., Raviolo, P. A., Pellegrini, L. F., and de Oliveira Júnior, S., 2010, "Exergy and Thermoeconomic Analysis of a Turbofan Engine During a Typical Commercial Flight," Energy, **35**(2), pp. 952–959.

[3] Denholm, P., O'Connell, M., Brinkman, G., and Jorgenson, J., 2015, "Overgeneration from Solar Energy in California: A Field Guide to the Duck Chart," Technical Report NREL/TP-6A20-65023, Contract No. DE-AC36-08GO28308.

[4] McKinsey & Co., 2019, https://www.mckinsey.com/~/media/mckinsey/industries/oil%20and%20gas/our%20insights/global%20energy%20perspective%202019/mckinsey-energy-insights-global-energy-perspective-2019_reference-case-summary.ashx.

[5] Khalid, S. J., and Hearne, R. E., 1980, "Enhancing Dynamic Model Fidelity for Improved Prediction of Turbofan Engine Transient Performance," 16th Joint Propulsion Conference, Hartford, CT, June 30–July 2.

[6] Pilidis, P., and Macallum, N. R. L., 1986, "The Effect of Heat Transfer on Turbine Performance," Proceedings of the ASME 1986 International Gas Turbine Conference and Exhibit. Volume 1: Turbomachinery, Dusseldorf, Germany, June 8–12, 86-GT-275.

[7] Nielsen, A. E., Moll, C. W., and Staudacher, S., 2005, "Modeling and Validation of the Thermal Effects on Gas Turbine Transients," ASME J. Eng. Gas Turbines Power, **127**(3), pp. 564–572.

[8] Selvam, K., De Prosperis, R., and Vanga, N. R., 2014, "Transient Thermal Analysis of Gas Turbine Shut Down Physics: Normal and Forced Cooling," Proceedings of the ASME 2014 International Mechanical Engineering Congress and Exposition, Montreal, Quebec, Canada, Nov. 14–20, IMECE2014-38164.

[9] Bunker, R. S., 2017, "Evolution of Turbine Cooling," Proceedings of ASME Turbo Expo 2017: Turbomachinery Technical Conference and Exposition, Charlotte, NC, June 26–30, GT2017-63205.

[10] Siroka, S., Monge-Concepción, I, Berdanier, R. A., Barringer, M. D., and Thole, K. A., 2021, "Correlating Cavity Sealing Effectiveness to Time-Resolved Rim Seal Events in the Presence of Vane Trailing Edge Flow," Proceedings of ASME Turbo Expo 2021 Turbomachinery Technical Conference and Exposition, Virtual, Online, June 7–11, GT2021-59285.

[11] Monge-Concepción, I., Siroka, S., Berdanier, R. A., Barringer, M. D., Thole, K. A., and Robak, C., 2021, "Unsteady Turbine Rim Sealing and Vane Trailing Edge Flow Effects," Proceedings of ASME Turbo Expo 2021 Turbomachinery Technical Conference and Exposition, Virtual, Online, June 7–11.

[12] Johnson, B. V., Mack, G. J., Paolillo, R. E., Daniels, W. A., Johnson, B., Beach, W. P., and Daniels, W., 1994, "Turbine Rim Seal Gas Path Flow Ingestion Mechanisms," 30th Joint Propulsion Conference, Indianapolis, IN, June 27–29, AIAA-94-2703.

[13] Clark, K., Barringer, M., Johnson, D., Thole, K., Grover, E., and Robak, C., 2017, "Effects of Purge Flow Configuration on Sealing Effectiveness in a Rotor-Stator Cavity," Proceedings of ASME Turbo Expo 2017: Turbomachinery Technical Conference and Exposition, Charlotte, NC, June 26–30, GT2017-63910.

[14] Berdanier, R. A., Monge-Concepción, I., Knisely, B. F., Barringer, M. D., Thole, K. A., and Grover, E. A., 2019, "Scaling Sealing Effectiveness in a Stator–Rotor Cavity for Differing Blade Spans," ASME J. Turbomach., **141**(5), p. 051007.

[15] Berdanier, R. A., DeShong, E. T., Thole, K. A., and Robak, C., 2021, "Evaluating the Effects of Transient Purge Flow on Stator-Rotor Seal Performance," ASME J. Turbomach., **143**(2), p. 021006.

[16] May, D., and Chew, J. W., 2010, "Response of a Disk Cavity Flow to Gas Turbine Engine Transients," Proceedings of ASME Turbo Expo 2010: Power for Land, Sea and Air, Glasgow, UK, June 14–18, GT2010-22824.

[17] Hualca, F. P., Horwood, J. T. M., Sangan, C. M., Lock, G. D., and Scobie, J. A., 2019, "The Effect of Vanes and Blades on Ingress in Gas Turbines," Proceedings of ASME Turbo Expo 2019: Turbomachinery Technical Conference and Exposition, Phoenix, AZ, June 17–21, GT2019-90987.

[18] Scobie, J. A., Sangan, C. M., Owen, J. M., Wilson, M., and Lock, G. D., 2014, "Experimental Measurements of Hot Gas Ingestion Through Turbine Rim Seals at Off-Design Conditions," Proc. Inst. Mech. Eng. J. Power Energy, **228**(5), pp. 491–507.

[19] Graikos, D., Carnevale, M., Sangan, C., Lock, G., and Scobie, J., 2021, "Influence of Flow Coefficients on Ingress Through Turbine Rim Seals of Flow Coefficient on Ingress Through Turbine Rim Seals," ASME J. Eng. Gas Turbines Power, **143**(11), p. 111010.

[20] Patinios, M., Scobie, J. A., Sangan, C. M., and Lock, G. D., 2017, "Performance of Rim-Seals in Upstream and Downstream Cavities Over a Range of Flow Coefficients," Int. J. Turbomach. Propuls. Power, **2**(4), p. 287.

[21] Popovic, I., and Hodson, H. P., 2013, "The Effects of a Parametric Variation of the Rim Seal Geometry on the Interaction Between Hub Leakage and Mainstream Flows in High Pressure Turbines," ASME J. Eng. Gas Turbines Power, **135**(11), p. 112501.

[22] Scobie, J. A., Sangan, C. M., Owen, J. M., and Lock, G. D., 2016, "Review of Ingress in Gas Turbines," ASME J. Eng. Gas Turbines Power, **138**(12), p. 120801.

[23] Owen, J. M., 1989, "An Approximate Solution for the Flow Between a Rotating and a Stationary Disc," ASME J. Turbomach., **111**(3), pp. 323–332.

[24] Owen, J. M., 2011, "Prediction of Ingestion Through Turbine Rim Seals—Part I: Rotationally Induced Ingress," ASME J. Turbomach., **133**(3), p. 031005.

[25] Owen, J. M., 2011, "Prediction of Ingestion Through Turbine Rim Seals—Part II: Externally Induced and Combined Ingress," ASME J. Turbomach., **133**(3), p. 31006.

[26] Phadke, U. P., and Owen, J. M., 1988, "Aerodynamic Aspects of the Sealing of Gas-Turbine Rotor-Stator Systems. Part 2: The Performance of Simple Seals in a Quasi-Axisymmetric External Flow," Int. J. Heat Fluid Flow, **9**(2), pp. 98–105.

[27] Gentilhomme, O., Hills, N. J., Turner, A. B., and Chew, J. W., 2003, "Measurement and Analysis of Ingestion Through a Turbine Rim Seal," J. Turbomach, **125**(3), pp. 505–512.

[28] Cao, C., Chew, J. W., Millington, P. R., and Hogg, S. I., 2003, "Interaction of Rim Seal and Annulus Flows in an Axial Flow Turbine," Proceedings of ASME Turbo Expo 2003 Power for Land, Sea, and Air, Atlanta, GA, June 16–19, GT2003-38368.

[29] Gao, F., Chew, J. W., and Marxen, O., 2020, "Inertial Waves in Turbine Rim Seal Flows," Phys. Rev. Fluids, **5**(2), p. 024802.

[30] Rabs, M., Benra, F. K., Dohmen, H. J., and Schneider, O., 2009, "Investigation of Flow Instabilities Near the Rim Cavity of a 1.5 Stage Gas Turbine," Proceedings of ASME Turbo Expo 2009: Power for Land, Sea and Air, Orlando, FL, June 8–12.

[31] Beard, P. F., Gao, F., Chana, K. S., and Chew, J., 2017, "Unsteady Flow Phenomena in Turbine Rim Seals," ASME J. Eng. Gas Turbines Power, **139**(3), p. 032501.

[32] Lei, X. I. E., Qiang, D. U., Guang, L. I. U., Zengyan, L., and Ran, R. E. N., 2021, "Investigation on Unsteady Flow Characteristics in Axial Rim Seal," Proceedings of ASME Turbo Expo 2021 Turbomachinery Technical Conference and Exposition, Virtual, Online, June 7–11, GT2021-58822..

[33] Robak, C. W., Faghri, A., and Thole, K. A., 2019, "Analysis of Gas Turbine Rim Cavity Ingestion With Axial Purge Flow Injection," Proceedings of ASME Turbo Expo 2019: Turbomachinery Technical Conference and Exposition, Phoenix, AZ, June 17–21.

[34] Barringer, M., Coward, A., Clark, K., Thole, K. A., Schmitz, J., Wagner, J., Hartford, E., Alvin, M. A., Burke, P., and Dennis, R., 2014, "The Design of a Steady Aero Thermal Research Turbine (START) for Studying Secondary Flow Leakgaes and Airfoil Heat Transfer," Proceedings of ASME Turbo Expo 2014: Turbine Technical Conference and Exposition, Dusseldorf, Germany, June 16–20, GT2014-25570.

[35] Monge-Concepción, I., Berdanier, R. A., Barringer, M. D., Thole, K. A., and Robak, C., 2020, "Evaluating the Effect of Vane Trailing Edge Flow on Turbine Rim Sealing," ASME J. Turbomach., **142**(8), p. 081001.

[36] Clark, K., Barringer, M. D., Thole, K. A., Clum, C., Hiester, P., Memory, C., and Robak, C., 2016, "Using a Tracer Gas to Quantify Sealing Effectiveness for Engine Realistic Rim Seals," Proceedings of ASME Turbo Expo 2016: Turbomachinery Technical Conference and Exposition, Seoul, South Korea, June 13–17.

[37] Sangan, C. M., Pountney, O. J., Zhou, K., Wilson, M., Michael Owen, J., and Lock, G. D., 2012, "Experimental Measurements of Ingestion Through Turbine Rim Seals—Part I: Externally Induced Ingress," ASME J. Turbomach., **135**(2), p. 021012.

[38] Figiola, R. S., and Beasley, D. E., 2014, Theory and Design for Mechanical Measurements, 2nd ed., John Wiley & Sons, Inc, Hoboken, NJ.

[39] DeShong, E. T., Peters, B., Berdanier, R. A., Thole, K. A., Paynabar, K., and Gabraeel, N., 2021, "Correlating Time-Resolved Pressure Measurements With Rim Sealing Effectiveness for Real-Time Turbine Health Monitoring," Proceedings of ASME Turbo Expo 2021 Turbomachinery Technical Conference and Exposition, Virtual, Online, June 7–11, GT2021-59586.

[40] Sangan, C. M., Pountney, O. J., Zhou, K., Owen, J. M., Wilson, M., and Lock, G. D., 2012, "Experimental Measurements of Ingestion Through Turbine Rim Seals—Part II: Rotationally Induced Ingress," ASME J. Turbomach., **135**(2), p. 021013.